

Amorphization of the thermal conductivity in crystalline half-Heusler superlattices

E. Chavez-Angel^{1,*†}, N. Reuter^{1*}, P. Komar^{1,2‡}, S. Heinz^{1,2}, U. Kolb^{3,4}, H.-J. Kleebe⁴ and G. Jakob^{1,2}

¹ Institut für Physik, Johannes Gutenberg Universität Mainz, Staudingerweg 7, 55128 Mainz, Germany.

² Graduate School Materials Science in Mainz, Staudingerweg 9, 55128 Mainz, Germany

³ Institute of Inorganic and Analytical Chemistry, Johannes Gutenberg Universität Mainz, Duesbergweg 10-14, 55128 Mainz, Germany.

⁴ Institute of Applied Geosciences, TU Darmstadt, Schnittspahnstraße 9, 64287 Darmstadt, Germany.

E-mail corresponding author: emigdio.chavez@icn2.cat

Keywords: Ultralow thermal conductivity, superlattices, amorphous limit of thermal conductivity

The quest to improve the thermoelectric figure of merit has mainly followed the roadmap of lowering the thermal conductivity while keeping unaltered the power factor of the material. Ideally an electron-crystal phonon-glass system is desired. In this work, we report an extraordinary reduction of the cross-plane thermal conductivity in crystalline (TiNiSn):(HfNiSn) half-Heusler superlattices. We create SLs with thermal conductivities below the effective amorphous limit, which is kept in a large temperature range (120-300 K). We measured thermal conductivity at room temperature values as low as $0.75 \text{ W m}^{-1} \text{ K}^{-1}$, the lowest thermal conductivity value reported so far for half-Heusler compounds. By changing the deposition conditions, we also demonstrate that the thermal conductivity is highly impacted by the way the single segments of the superlattice grow. These findings show a huge potential for thermoelectric generators where an extraordinary reduction of the thermal conductivity is required but without losing the crystal quality of the system

* Equally contributing authors

Current address

† Catalan Institute of Nanoscience and Nanotechnology (ICN2), CSIC and BIST, Campus UAB, Bellaterra, 08193 Barcelona, Spain.

‡ Photonics Group, Institute of Physics, Lodz University of Technology, Wólczańska 219, 90-924 Łódź, Poland.

1. Introduction

Understanding of heat propagation and the ability to tune the thermal properties constitute a topic of continuous and active research motivated by the increasing importance of thermal management and ways to recover waste heat energy as it is the case for the thermoelectric industry. This renewed interest in thermal management has introduced a number of novel concepts and ideas including: thermocrystals¹, thermal-cloaking, -transistors, -diodes and -memories²⁻⁹, phonon-mean-free-path spectroscopy^{10,11}, among others.

The control of phonon propagation, the main heat carriers in semiconductors and insulators, is a crucial requirement for thermoelectric generation. Ideally, a material with thermal properties of an amorphous state (phonon glass) and electronic properties associated with good single-crystal semiconductor (electron crystal) are desired.¹² Materials very low thermal conductivity, k , are also needed in other applications such as: thermal barrier coatings for gas turbine engines and thermal data storage devices.¹³

The lowest k in crystalline systems is achievable through alloy scattering, or the so-called alloy limit. But, the introduction of an extra scattering mechanisms, e.g., nanostructures, can exceed this limit. The use of superlattices¹⁴⁻¹⁷ and embedded nanoparticles¹⁸ have demonstrated to be a good way to reduce k below the alloy limit, while maintaining the crystal quality of the material. The introduction of more and more scattering events can reduce even further this limit reaching its second minima: the amorphous limit. In this context, recent experiments showed that, by introducing small-periods in SLs, ultralow k values below the amorphous limit can be achieved.¹⁹⁻²¹ Costescu *et al.*¹⁹ and Pernot *et al.*²⁰ measured cross plane thermal conductivity values (k_{\perp}) below the amorphous limit of Al₂O₃ and Si in Al₂O₃:W and SiGe:Si SLs, respectively. Niemelä *et al.* also overtook the amorphous limit of TiO₂ using organic-inorganic (TiO₂):(Ti—O—C₆H₄—O) SLs. Moreover, Chiritescu *et al.*²² also measured ultralow k_{\perp} in layered WSe₂ thin films. k_{\perp} values below the amorphous limit of WSe₂ crystal was achieved by controlling both order and disorder in the thin films.

In SLs, thus, it is natural to think that the smaller period length (L), the smaller k_{\perp} . However, several theoretical^{15,23–25} and experimental^{17,26,27} reports have shown that for very thin L the k_{\perp} increases. In such limit, phonons experience the material as if it was composed of enlarged unit cells given by the size of L . The SL is seen as one homogenous material and the phonon transport is considered coherent.²⁸ The transition between coherent-incoherent (wave-particle) transport is observed as a minimum in the thermal conductivity, k_{\perp} as a function of L ^{17,26}. This effect comes from the competition between phonons diffusively scattered at each interface and the band-folded ones. Another fingerprint of coherent thermal transport was proposed by Luckyanova *et al.*²⁸, namely, a linear dependence of k_{\perp} with respect to the number of periods as indicator of coherent thermal transport through the SL. This arises when the phonon mean free paths (MFPs) are equal to the total thickness of the SL (d) leading to the linear dependence of k_{\perp} on the number of periods.

In this work we report ultralow thermal conductivity in rough (TiNiSn):(HfNiSn) (with abbreviation (TNS):(HNS)) half-Heusler SLs. The period length of the SLs has been chosen to match crossover from incoherent to coherent transport in HH SLs.²⁹ The measured k_{\perp} showed values below the amorphous limit of the effective material. As far as we know, these results are the lowest experimental values reported so far for any kind of half-Heusler (HH) compounds.

2. Previous results

The HH compounds investigated here are n-type narrow-band-gap semiconductors with quite large Seebeck coefficient and electrical conductivity.^{30,31} However, the relatively high thermal conductivity still limits their thermoelectric performance and, hence, the industrial commercialization. For this reason, our previous studies were focused on the k reduction through SL structuration. We designed three different experiments to study the impact of the period length^{29,32} and the period composition³³ on the electrical and thermal properties of HH SLs. Our findings revealed a room temperature crossover from incoherent to coherent thermal

transport in HH SLs. The k_{\perp} vs L exhibited a continuous diminution of k_{\perp} as L decreases, showing a minimum of $k_{\perp} = 1.11 \pm 0.06 \text{ W K}^{-1} \text{ m}^{-1}$ at $L \sim 3.2 \text{ nm}$. At smaller L the k_{\perp} rises up entering in the coherent regime.^{29,32}

3. Experimental results and discussion

In this work, we have taken a different experimental approach to study the heat transport through the SL. Instead of fabricating smooth and defect-free SLs, we have deteriorated the quality of the interfaces by changing the deposition conditions. We used DC magnetron sputtering to fabricate eight (TNS):(HNS) SLs with period thicknesses ranging from $2.9 \text{ nm} < L < 4.8 \text{ nm}$. The L was determined from the best fit of the X-ray diffractograms using CADEM: calculate X-ray diffraction of epitaxial multilayers.³⁴ Five SLs were grown with the same number of periods $N = 37$ (S_1, S_2, S_3, S_7 and S_8 , respectively). Other three samples were deposited with different number of periods $N = 111$ (S_4, S_6) and 148 (S_5). All these samples, except S_1 (homogeneous-growth), were grown 30 mm away from the center of the cathodes in the inhomogeneous part of the plasma cloud (inhomogeneous-growth). Two different deposition conditions were used here. S_1, S_2, S_6, S_7 and S_8 were grown at low gas pressure and cathode power (low rate), while S_3, S_4 and S_5 were grown at high gas pressure and cathode power (high rate). The surface roughness was determined from the root mean square of a two dimensional power spectral density plot of the sample surface measured by atomic force microscopy, AFM. For convenience, the AFM surface-roughness will be referred simply as roughness (η). A detailed description of the sample fabrication can be found in the supporting information.

A cross-sectional transmission electron microscope (TEM) image of one SL with a roughness of $\eta = 5.9 \text{ nm}$ and period thickness $L = 4.5 \text{ nm}$ is displayed in **Figure 1a**. As one can see in the inset of **Figure 1a**, there is an intermixing of the SL layers, however, the SL still keeps the crystal quality as is shown in the rocking curve in **Figure 1b** and its inset. In addition, the

presence of the (002) and (004) film reflections around $2\theta = 30^\circ$ and 60° , respectively, confirm the crystallinity of all the samples (see **Figure S3**, **S4**, and **S6** in the supporting information).

The cross-plane thermal conductivity was measured using well-known three-omega (3ω) method^{35,36} in the differential configuration.^{37,38} **Figure 2a** and **2b** show the temperature and the η dependence of the k_\perp of the S_1 - S_3 SLs, respectively.

First, we will focus on S_1 and S_2 , grown under the same low sputtering rates but at different distance of the cathodes. The homogeneously-grown SL (S_1) shows significantly higher k_\perp than the inhomogeneous SL (S_2) above 120 K. It appears that the difference in period lengths ($L_1 = 2.9$ nm and $L_2 = 3.5$ nm for S_1 and S_2 , respectively) may explain this finding. However, in a previous work, we found that the k_\perp decreases as period length decreases achieving a minimum value $k_\perp \approx 1.11$ W K⁻¹ m⁻¹ at $L \approx 3.2$ nm.²⁹ Then, as both period lengths of the SLs are located around this minimum, the k_\perp should be almost identical. Therefore, the difference in k_\perp cannot be associated exclusively to SL period. Moreover, due to the change of the deposition conditions and the correspondingly higher roughness (S_3), the k_\perp decreases even more reaching values as low as the theoretical amorphous limit of HNS and below the amorphous limit of an effective material.³⁹ This behavior is preserved along a vast temperature range $100 < T < 300$ K as is displayed in **Figure 2a**. Here, it is natural to think that an amorphization of the SL due the modification of the deposition conditions could also explain such low values. However, as displayed in the **Figure 1b**, the sharpness of the rocking curve as well as the presence of the typical (002) and (004) peaks of HH compounds in XRD diffractograms (see **Figure S3c** of the supporting information) indicate a high crystal quality. Moreover, the FWHM of the rocking curve of S_3 ($\Gamma = 1.08^\circ$) is smaller than S_1 ($\Gamma = 1.31^\circ$) and S_2 ($\Gamma = 1.51^\circ$), i.e., S_3 is crystallographically superior to S_1 and S_2 and k_\perp should be even

higher. Thus, the extremely low k_{\perp} values shown by S_3 can be directly associated to the η that is comparable to L in case of S_3 .

Figure 3a shows the k_{\perp} as function of number of periods corresponding to the samples S_3 , S_4 and S_5 , respectively. All these samples were grown under the same deposition condition as S_3 and just the total number of periods was varied. The period length in this case should be similar but it is possible to see a shift of the satellite peaks (**Figure S4** supporting information). The calculated period length was found $L = 3.9$ nm and 4.8 nm for S_4 and S_5 , respectively.

From **Figure 3a**, one sees that k_{\perp} rises continuously at 250 K and at 170 K similarly to the behaviour observed by Luckyanova³⁰. While for 100 K the k_{\perp} seems to be constant for thicker samples. The nearly linear dependence k_{\perp} on the number of periods seems that part of the heat is transported still by “coherent phonons” with mean free path in the order of the sample thicknesses. Other interpretation of this phenomena can be associated to epitaxial quality of the thicker samples. The inset of **Figure 1b** shows very sharp FWHM S_4 ($\Gamma = 0.77^\circ$) and S_5 ($\Gamma = 0.75^\circ$). This means that both S_4 and S_5 have superior epitaxial quality than S_3 . As this effect may also play a role here, the k_{\perp} as function of FWHM is plotted in **Figure 4a**. From the graph it is not possible to observe clear correlation between k_{\perp} and the FWHM. But, if we paid attention to the samples grown under the same deposition conditions, there is apparently a correlation between the thermal conductance, $k_{\perp} \cdot d$ (where d is the total thickness of each SL), and the FWHM (see **Figure 4b**). Nevertheless the strong reduction of the k_{\perp} , by more than 60%, shown by S_3 may indicate partly the cut off of coherent phonon transport by the limiting total film thickness.

The other important parameter that we have to take into account is the surface roughness, which rises significantly with the number of periods. In contrast to previous cases, here the surface roughness of S_4 and S_5 is $\eta \sim 28$ nm, which is six times larger than the L of the SL.

Such huge η should also impact on the k_{\perp} reducing it even more, in spite of that, we observe that the experimental k_{\perp} is still increasing. This counterintuitive behavior of k_{\perp} can be explained in terms of crystal domains. Due to the high deposition rate, the SL tends to form pillar-like structures with lateral size ~ 200 nm (see **Figure S5** supporting information). Then, as the lateral sizes of these pillars are larger than the period length of the SL, the thermal phonons can propagate more easily through SL interfaces. Similar behavior of k_{\perp} can be also observed for the SLs grown at low deposition rate (see **Figure 3b**). Again, we kept high crystal quality showing sharp FWHM of the samples S_2 ($\Gamma = 1.53^\circ$) and S_6 ($\Gamma = 1.00^\circ$). We can notice that the k_{\perp} rises up for larger number of periods (S_6 , $N = 111$ and $L = 4.5$ nm).

Another interesting question concerning reduction of the thermal conductivity is, whether it is caused just by the fact that the one single component of the SL grows in a special way or if it is caused by the interaction of both components. To test this effect a double substrate holder was used for deposition. On this holder, there is room for two substrates lying side by side. So, during the deposition processes, one substrate is a little bit closer to the HNS and the other to the TNS, respectively. As the samples were grown in the inhomogeneous region of the plasma cloud, one of the SLs will contain a little bit more TNS or HNS per period than the other. This effect can be appreciated in XRD diffractograms displayed in the **Figure S6** in the supporting information. The XRD diffractogram shows that the maxima of (002) HH peaks are shifted. As expected, the sample closer to HNS cathode (S_6) has a maximum at 29.4° which is closer to (002) peak of HNS (29.36°). While the sample closer to TNS cathode (S_7) has a maximum at 29.9° which is closer to (002) peak of TNS (30.06°). The rocking curves of both samples show an equal FWHM value of 1.21° . Here we focused on SLs having the same number of periods, which were grown with low sputtering rate to minimize the impact of the roughness. In **Figure 3c**, the k_{\perp} of S_6 and S_7 are compared to the SL grown using single sample-holder S_2 . It is clear that the sample that contained more TNS (S_6) has higher thermal conductivity than

the sample that contained more HNS (S_7) and the single sample-holder (S_2). Similar results we also observed in our previous investigation in HHs SLs. Where we found a minimum of the k_{\perp} $\sim 1.39 \text{ W K}^{-1} \text{ m}^{-1}$ for SL having the same amount of each material.³³

Coming back to the idea of coherent transport, while it is interesting to speak about of a possible coherent transport in rough SLs, we cannot proof that the heat transport is influenced by coherent phonons just based on the nearly-linear dependence of k_{\perp} on the number of periods. Other mechanism such material intermixing, different degree of interface roughness and privileged growth of one of the constituent materials of the SL could also explain this linear dependence of k_{\perp} .

3. Conclusions

In this work we found out that the samples that were grown in the inhomogeneous region of the deposition cloud exhibited significantly lower thermal conductivity than the sample grown at the homogenous part. The thermal conductivity can be reduced even below the amorphous limit by using higher gas pressure and cathode power for deposition process. This is an outstanding result because it means that a solid body with good crystalline qualities (as implied by the narrow rocking curves) has a lower thermal conductivity than it should have in amorphous state. We also observed experimentally a linear-like increase of k_{\perp} as a function of the number of periods for SL grown under variable deposition conditions. While this behavior has been reported before as coherent transport, we cannot prove that this is the case in this work. Other parameters such as the degree of intermixing, interface roughness and crystal quality may also play a role. Furthermore, we have also demonstrated that the thermal conductivity is influenced by the way in which one of the single components grows within the inhomogeneous region. Finally, our findings show a large potential for thermoelectric generators where a huge reduction of k is required but without losing the crystal quality of the system.

Acknowledgements

We gratefully acknowledge financial support by the Deutsche Forschungsgemeinschaft, DFG, Germany, [Grants No. Ja821/4 within SPP1386 (Nanostructured Thermoelectric Materials) and No. Ja821/7-1 within SPP1538 (Spin Caloric Transport)] and the Graduate School of Excellence Material Science in Mainz (GSC266).

References

- (1) Maldovan, M. Narrow Low-Frequency Spectrum and Heat Management by Thermocrystals. *Phys. Rev. Lett.* **2013**, *110* (2), 25902.
- (2) Guenneau, S.; Amra, C.; Veynante, D. Transformation Thermodynamics: Cloaking and Concentrating Heat Flux. *Opt. Express* **2012**, *20* (7), 8207–8218.
- (3) Han, T.; Bai, X.; Thong, J. T. L.; Li, B.; Qiu, C.-W. Full Control and Manipulation of Heat Signatures: Cloaking, Camouflage and Thermal Metamaterials. *Adv. Mater.* **2014**, *26* (11), 1731–1734.
- (4) Xu, H.; Shi, X.; Gao, F.; Sun, H.; Zhang, B. Ultrathin Three-Dimensional Thermal Cloak. *Phys. Rev. Lett.* **2014**, *112* (5), 54301.
- (5) Ben-Abdallah, P.; Biehs, S.-A. Near-Field Thermal Transistor. *Phys. Rev. Lett.* **2014**, *112* (4), 44301.
- (6) Li, B.; Wang, L.; Casati, G. Thermal Diode: Rectification of Heat Flux. *Phys. Rev. Lett.* **2004**, *93* (18), 184301.
- (7) Wang, L.; Li, B. Thermal Memory: A Storage of Phononic Information. *Phys. Rev. Lett.* **2008**, *101* (26), 267203.
- (8) Kubytskyi, V.; Biehs, S.-A.; Ben-Abdallah, P. Radiative Bistability and Thermal Memory. *Phys. Rev. Lett.* **2014**, *113* (7), 74301.
- (9) Elzouka, M.; Ndao, S. Near-Field NanoThermoMechanical Memory. *Appl. Phys. Lett.* **2014**, *105* (24), 243510.
- (10) Minnich, A. J. Determining Phonon Mean Free Paths from Observations of Quasiballistic Thermal Transport. *Phys. Rev. Lett.* **2012**, *109* (20), 205901.

(11) Maasilta, I.; Minnich, A. J. Heat under the Microscope. *Phys. Today* **2014**, *67* (8), 27–32.

(12) Slack, G. A. *CRC Handbook of Thermoelectrics*; Rowe, D. M., Ed.; CRC Press: Boca Raton, 1995.

(13) Goodson, K. E. MATERIALS SCIENCE: Ordering Up the Minimum Thermal Conductivity of Solids. *Science* **2007**, *315*, 342–343.

(14) Capinski, W. S.; Maris, H. J.; Ruf, T.; Cardona, M.; Ploog, K.; Katzer, D. S. Thermal-Conductivity Measurements of GaAs/AlAs Superlattices Using a Picosecond Optical Pump-and-Probe Technique. *Phys. Rev. B* **1999**, *59* (12), 8105–8113.

(15) Koh, Y. K.; Cao, Y.; Cahill, D. G.; Jena, D. Heat-Transport Mechanisms in Superlattices. *Adv. Funct. Mater.* **2009**, *19* (4), 610–615.

(16) Chen, P.; Katcho, N. A.; Feser, J. P.; Li, W.; Glaser, M.; Schmidt, O. G.; Cahill, D. G.; Mingo, N.; Rastelli, A. Role of Surface-Segregation-Driven Intermixing on the Thermal Transport through Planar Si/Ge Superlattices. *Phys. Rev. Lett.* **2013**, *111* (11), 115901.

(17) Ravichandran, J.; Yadav, A. K.; Cheaito, R.; Rossen, P. B.; Soukiassian, A.; Suresha, S. J.; Duda, J. C.; Foley, B. M.; Lee, C.-H.; Zhu, Y.; et al. Crossover from Incoherent to Coherent Phonon Scattering in Epitaxial Oxide Superlattices. *Nat. Mater.* **2013**, *13* (2), 168–172.

(18) Woochul Kim; Singer, S.; Majumdar, A.; Zide, J.; Gossard, A.; Shakouri, A. Role of Nanostructures in Reducing Thermal Conductivity below Alloy Limit in Crystalline Solids. In *ICT 2005. 24th International Conference on Thermoelectrics, 2005.*; IEEE, 2005; pp 9–12.

(19) Costescu, R. M.; Cahill, D. G.; Fabreguette, F. H.; Sechrist, Z. A.; George, S. M. Ultra-Low Thermal Conductivity in W/Al₂O₃ Nanolaminates. *Science* **2004**, *303* (5660), 989–990.

(20) Pernot, G.; Stoffel, M.; Savic, I.; Pezzoli, F.; Chen, P.; Savelli, G.; Jacquot, A.; Schumann, J.; Denker, U.; Mönch, I.; et al. Precise Control of Thermal Conductivity at the Nanoscale through Individual Phonon-Scattering Barriers. *Nat. Mater.* **2010**, *9* (6), 491–495.

(21) Niemelä, J.-P.; Giri, A.; Hopkins, P. E.; Karppinen, M. Ultra-Low Thermal Conductivity in TiO_2 :C Superlattices. *J. Mater. Chem. A* **2015**, *3* (21), 11527–11532.

(22) Chiritescu, C.; Cahill, D. G.; Nguyen, N.; Johnson, D.; Bodapati, A.; Kebinski, P.; Zschack, P. Ultralow Thermal Conductivity in Disordered, Layered WSe₂ Crystals. *Science* **2007**, *315* (5810), 351–353.

(23) Garg, J.; Chen, G. Minimum Thermal Conductivity in Superlattices: A First-Principles Formalism. *Phys. Rev. B* **2013**, *87* (14), 140302.

(24) Wang, Y.; Huang, H.; Ruan, X. Decomposition of Coherent and Incoherent Phonon Conduction in Superlattices and Random Multilayers. *Phys. Rev. B* **2014**, *90* (16), 165406.

(25) Mizuno, H.; Mossa, S.; Barrat, J.-L. Beating the Amorphous Limit in Thermal Conductivity by Superlattices Design. *Sci. Rep.* **2015**, *5*, 14116.

(26) Venkatasubramanian, R. Lattice Thermal Conductivity Reduction and Phonon Localizationlike Behavior in Superlattice Structures. *Phys. Rev. B* **2000**, *61* (4), 3091–3097.

(27) Saha, B.; Koh, Y. R.; Comparan, J.; Sadasivam, S.; Schroeder, J. L.; Garbrecht, M.; Mohammed, A.; Birch, J.; Fisher, T.; Shakouri, A.; et al. Cross-Plane Thermal Conductivity of $(\text{Ti},\text{W})\text{N}/(\text{Al},\text{Sc})\text{N}$ Metal/semiconductor Superlattices. *Phys. Rev. B* **2016**, *93* (4), 45311.

(28) Luckyanova, M. N.; Garg, J.; Esfarjani, K.; Jndl, A.; Balsara, M. T.; Schmidt, A. J.; Minnich, A. J.; Chen, S.; Dresselhaus, M. S.; Ren, Z.; et al. Coherent Phonon Heat Conduction in Superlattices. *Science* **2012**, *338* (6109), 936–939.

(29) Hołuj, P.; Euler, C.; Balke, B.; Kolb, U.; Fiedler, G.; Müller, M. M.; Jaeger, T.; Chávez Angel, E.; Kratzer, P.; Jakob, G. Reduced Thermal Conductivity of TiNiSn/HfNiSn Superlattices. *Phys. Rev. B* **2015**, *92* (12), 125436.

(30) Poon, G. J. Electronic and Thermoelectric Properties of Half-Heusler Alloys. In *Semiconductors and semimetals: Recent trends in thermoelectric materials research II* Vol. 70; Tritt, T. M., Ed.; Academic Press, 2001; pp 37–75.

(31) Downie, R. A.; Barczak, S. A.; Smith, R. I.; Bos, J. W. G. Compositions and Thermoelectric Properties of XNiSn (X = Ti, Zr, Hf) Half-Heusler Alloys. *J. Mater. Chem. C* **2015**, *3* (40), 10534–10542.

(32) Komar, P.; Jaeger, T.; Euler, C.; Chávez Angel, E.; Kolb, U.; Müller, M. M.; Balke, B.; Aguirre, M. H.; Populoh, S.; Weidenkaff, A.; et al. Half-Heusler Superlattices as Model Systems for Nanostructured Thermoelectrics. *Phys. status solidi* **2015**, *213*, 732–738.

(33) Komar, P.; Chávez-Ángel, E.; Euler, C.; Balke, B.; Kolb, U.; Müller, M. M. ; Kleebe, H.-J.; Fecher, G. H.; Jakob, G. Tailoring of the Electrical and Thermal Properties Using Ultra-Short Period Non-Symmetric Superlattices. *APL Mater.* **2016**, *4* (10), 104902.

(34) Komar, P.; Jakob, G. CADEM : Calculate X-Ray Diffraction of Epitaxial Multilayers. *J. Appl. Crystallogr.* **2017**, *50* (1), 288–292.

(35) Cahill, D. G. Thermal Conductivity Measurement from 30 to 750 K: The 3ω Method. *Rev. Sci. Instrum.* **1990**, *61* (2), 802.

(36) Cahill, D. G. Erratum: “Thermal Conductivity Measurement from 30 to 750 K: The 3ω Method” [Rev. Sci. Instrum. 61, 802 (1990)]. *Rev. Sci. Instrum.* **2002**, *73* (10), 3701.

(37) Cahill, D.; Katiyar, M.; Abelson, J. Thermal Conductivity of a-Si:H Thin Films. *Phys. Rev. B* **1994**, *50* (9), 6077–6081.

(38) Kim, J. H.; Feldman, A.; Novotny, D. Application of the Three Omega Thermal Conductivity Measurement Method to a Film on a Substrate of Finite Thickness. *J.*

(39) Cahill, D. G.; Watson, S. K.; Pohl, R. O. Lower Limit to the Thermal Conductivity of Disordered Crystals. *Phys. Rev. B* **1992**, *46* (10), 6131–6140.

Figures

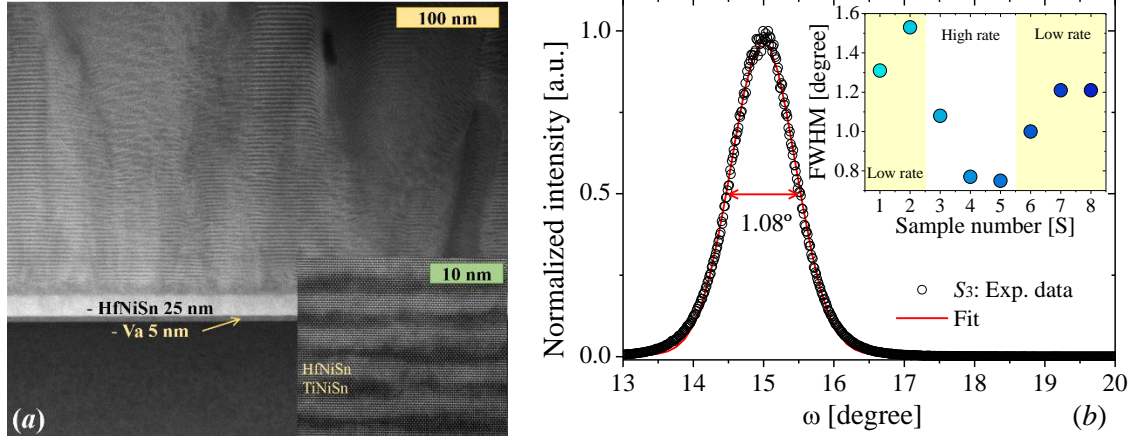


Figure 1. (a) Cross-sectional TEM image of 37 periods and $L \sim 4.5$ nm SL. (inset) High-Resolution TEM (HRTEM) image of one part of the SL. (b) Measured rocking curve of HfNiSn (002) peak of S3 SL. (inset) Full-width-half-maximum (FWHM or Γ) of the rocking curve of each sample investigated in this work.

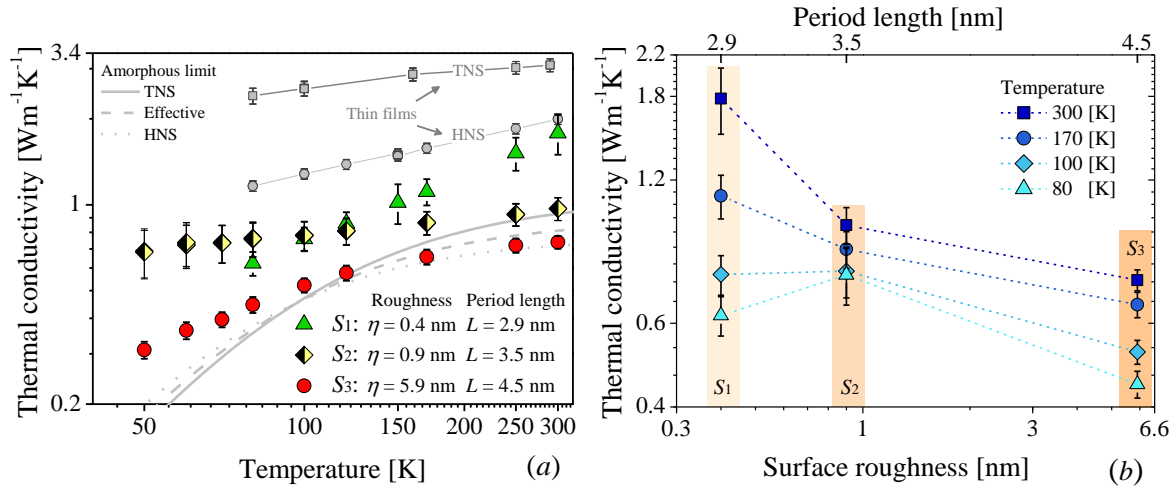


Figure 2 (a) Temperature dependence of the k_{\perp} of three different SLs (colored solid symbols) and of two 1000 nm thick TNS and HNS thin films (grey square and circle symbols, respectively). The solid and dotted grey lines represent the theoretical amorphous limit of TNS and HNS. The dashed grey line represents the amorphous limit of an effective material composed by mixture of both HHs. (b) Roughness dependence of the k_{\perp} at four different temperature

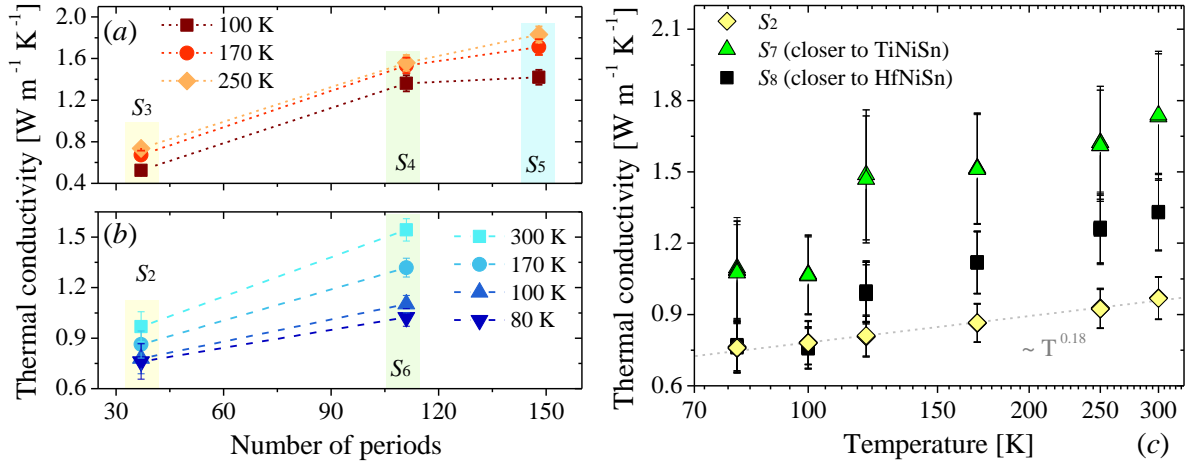


Figure 3 (a-b) Thermal conductivity vs number of periods measured at different temperatures for: SLs fabricated using **(a)** high and **(b)** low deposition rates, respectively. **(c)** Temperature dependence of the thermal conductivity for three different SLs grown at low deposition rates and using different sample-holders.

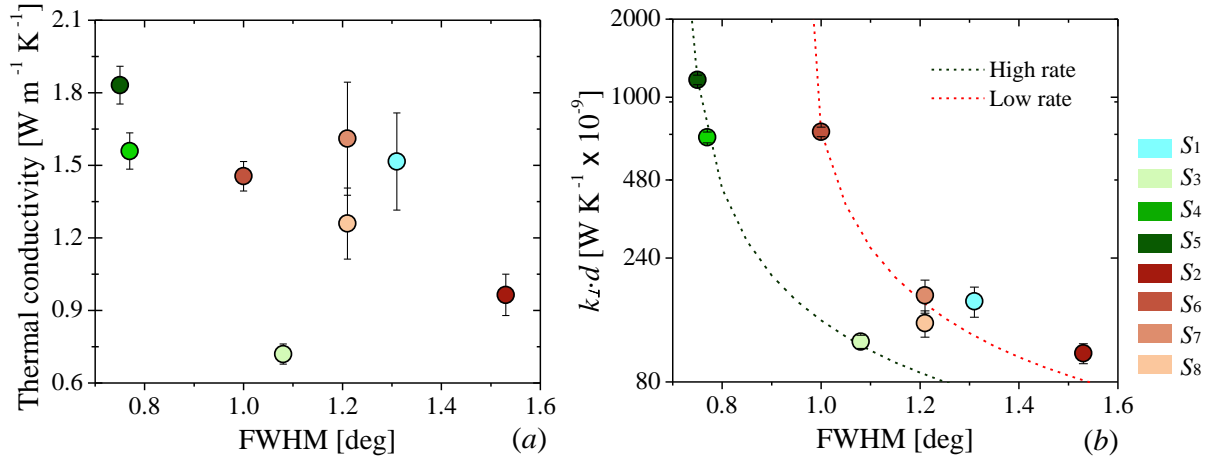


Figure 4 (a) Cross-plane thermal conductivity and **(b)** thermal conductance ($k_{\perp} \cdot d$) as a function of FWHM of the rocking curves. The dashed dark-green and red lines are used to guide the eye.

Supporting Information

Amorphization of the thermal conductivity in crystalline half-Heusler superlattices

E. Chavez-Angel^{1,*†}, N. Reuter^{1*}, P. Komar^{1,2,‡}, S. Heinz^{1,2}, U. Kolb^{3,4}, H.-J. Kleebe⁴ and G. Jakob^{1,2}

¹ Institut für Physik, Johannes Gutenberg Universität Mainz, Staudingerweg 7, 55128 Mainz, Germany.

² Graduate School Materials Science in Mainz, Staudingerweg 9, 55128 Mainz, Germany

³ Institute of Inorganic and Analytical Chemistry, Johannes Gutenberg Universität Mainz, Duesbergweg 10-14, 55128 Mainz, Germany.

⁴ Institute of Applied Geosciences, TU Darmstadt, Schnittspahnstraße 9, 64287 Darmstadt, Germany.

E-mail corresponding author: emigdio.chavez@icn2.cat

Keywords: Ultralow thermal conductivity, superlattices, amorphous limit of thermal conductivity

Nomenclature

		<i>Greek symbols</i>
<i>a</i>	Lattice constant [m]	δ Error deviation
AC	Alternating current	ϕ Phase lag
AFM	Atomic force microscopy	η Surface roughness [nm]
<i>b</i>	Half width of three-omega heater [m]	Λ Phonon mean free path [m]
<i>d</i>	Thickness of sample or distance to the centre of the cathode [m]	λ Thermal wavelength and/or wavelength of the heat carrier [m]
DC	Direct current	Θ_D Debye temperature [K]
<i>f</i>	Frequency [Hz]	ω Angular frequency ($2\pi f$) [rad s ⁻¹]
<i>h</i>	Planck constant [J s]	
<i>i</i>	Imaginary number	
<i>I</i>	Current [A]	<i>Subscripts</i>
<i>k</i>	Thermal conductivity [W K ⁻¹ m ⁻¹]	<i>app</i> Applied current [A]
<i>k_B</i>	Boltzmann constant [J K ⁻¹]	<i>c</i> Corrected temperature
<i>l</i>	Heater length [m]	<i>iso</i> Insolation layer
MFP	Mean free path	<i>f</i> Thin film
<i>N</i>	Number of periods	<i>h</i> heater
<i>n</i>	Number density of atoms [m ⁻³]	<i>L</i> Longitudinal polarization
P	Power [W]	<i>r</i> Reference film
<i>p</i>	Pressure [mbar]	<i>rel</i> Relative error deviation
<i>R</i>	Resistance [Ω]	<i>rms</i> Root mean square
SL	Superlattice	<i>S</i> Substrate
<i>T</i>	Temperature [K]	<i>SLs</i> Superlattices
<i>U</i>	Voltage [V]	<i>sys</i> Full system including insulation layer, film of interest, reference and the substrate
<i>v</i>	Sound velocity [m s ⁻¹]	<i>T</i> Transverse polarization
XRR	X-ray reflectivity	

* Equally contributing authors

Current address

† Catalan Institute of Nanoscience and Nanotechnology (ICN2), CSIC and BIST, Campus UAB, Bellaterra, 08193 Barcelona, Spain.

‡ Photonics Group, Institute of Physics, Lodz University of Technology, Wólczańska 219, 90-924 Łódź, Poland.

Supporting Information

Characterization techniques

For structural characterization we employed Cs corrected scanning transmission electron microscope (STEM), X-ray diffraction (XRD) and atomic force microscopy (AFM). The high resolution STEM (HR-STEM) measurements were performed on tripod polished samples using JEOL JEM ARM 200F operated at 200 kV, applying high angle annular dark field (HAADF) imaging. The crystallographic quality was determined based on θ - 2θ patterns and ω (rocking curve) scans recorded by a Bruker D8 Discovery X-ray diffractometer operated in Bragg-Brentano geometry. Surface roughness was measured by the root mean square (RMS) of a two dimensional power spectral density plot in a representative range of the sample's surface. It was recorded by Veeco Dimension 3100 setup, operated in the contact mode. The samples thickness were measured by using the same AFM equipment.

1. Fabrication process

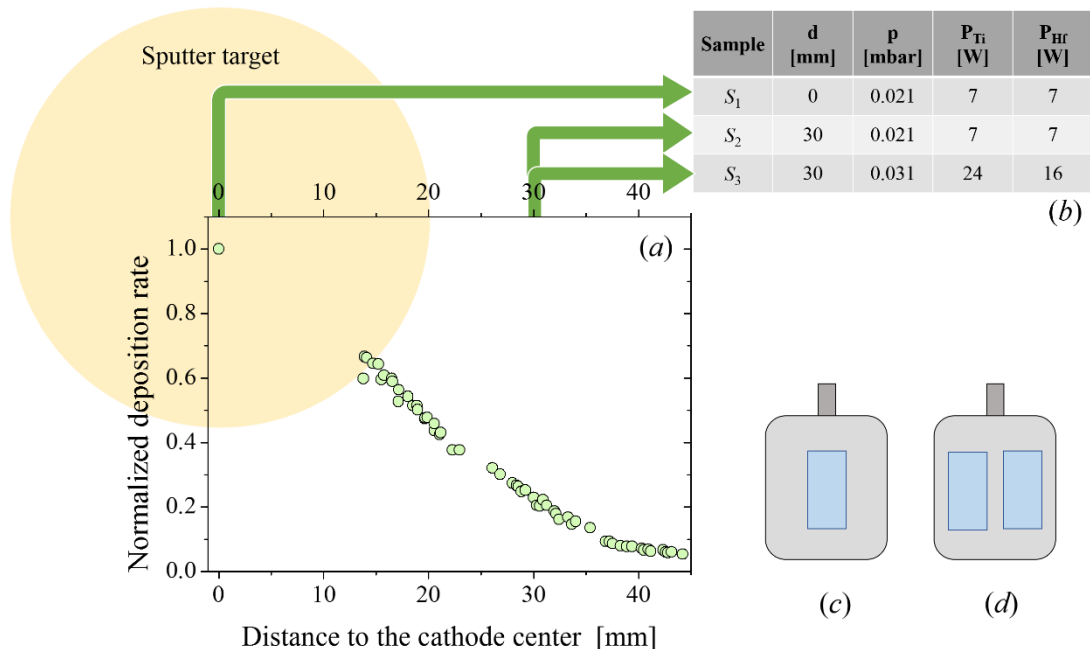


Figure S1 (a) Normalized deposition rate of the used TiNiSn and HfNiSn cathodes as a function of distance between cathode center line and MgO substrate center (b) The creation parameters for each of the three samples. (c)-(d) Sample holder for a single (c) and double (d) SL deposition.

The SLs were grown by DC magnetron sputtering processes on 10 mm×5 mm MgO substrates using a Vanadium (5 nm) and HfNiSn (25 nm) as a buffer layer at T = 520 °C. The deposition rate was measured using AFM and XRR. As it is displayed in Figure S1, the deposition rate depends on the distance between substrate and central axis of the cathode due to the spiral trajectories that the ionized gas atoms follow around the field lines of the inhomogeneous magnetic field during the sputtering process. The SLs were grown at two different positions in relation to the centre of the cathode using different gas pressure, cathode powers and sample holders.

Supporting Information

The first sample (S_1) was grown above the cathode centre at low Ar pressure ($p = 0.21$ mbar), low cathode powers ($P_{Ti} = P_{Hf} = 7$ W) and using a single sample holder (see **Figure S1 c**). The second sample (S_2) was deposited using the same growing conditions but 30 mm away from the centre of the cathode. The third sample (S_3) was grown at the same place of S_2 but with higher Ar pressure ($p = 0.21$ mbar) and cathode power ($P_{Ti} = 24$ W and $P_{Hf} = 16$ W). For these three samples (S_1 - S_3), we kept constant the total number of periods $N = 37$. Other two samples were also grown using the same deposition condition than S_3 but with different number of periods $N = 111$ (S_4) and 148 (S_5), respectively. In addition, other two samples were grown using the same deposition condition of S_3 but with a different sample holder allowing to place two substrates at the same time (see **Figure S1 d**). As one can see in the **Figure S2**, if we use the double sample holder it is clear to see that one of the substrate we will a little bit closer to one of the cathode. The thickness of all the samples presented in this work was measured by using AFM. A summary of the growth conditions is displayed in the **Table S1**.

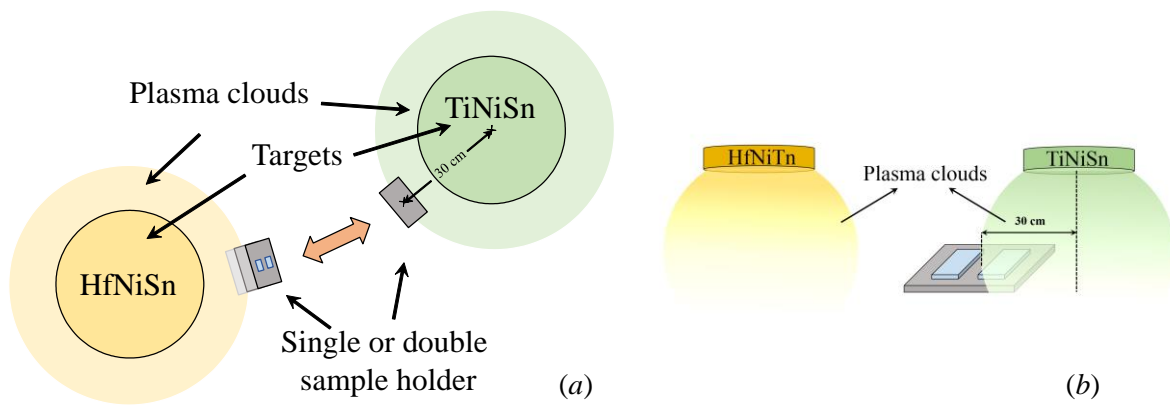


Figure S2 (a) and (b) schematic view of the sample deposition and the growth in the inhomogeneous part of the plasma cloud.

1.1 Surface and crystal structure analysis

By looking at the AFM surface scans, displayed in **Figure S3 g** to **i**, one can notice a remarkable difference between the samples at a microscopic scale. Clearly, the samples grown 30 mm away from the cathode are rougher than the ones grown when the sample holder was centred. Additionally, the gas pressure and the power applied to the cathodes have also an impact on the increase of the surface roughness of the samples, as it is shown in the **Figure S3 i**.

Regarding the XRD analysis, S_1 shows satellite peaks that are characteristic for SLs as shown in **Figure S3 a**. The satellite peaks of S_2 and S_3 are less pronounced and less symmetric as expected for samples that were sputtered at a place with spatially inhomogeneous deposition rates leading to unclear interfaces (see **Figure S3 b** and **c**, respectively). Consequently, the samples are definitely different in the SL structure. However, the crystal quality of all samples is similar as one can see in the Full-Width-Half-Maximum (FWHM) of rocking curves (**Figure S3 d** to **f**).

Supporting Information

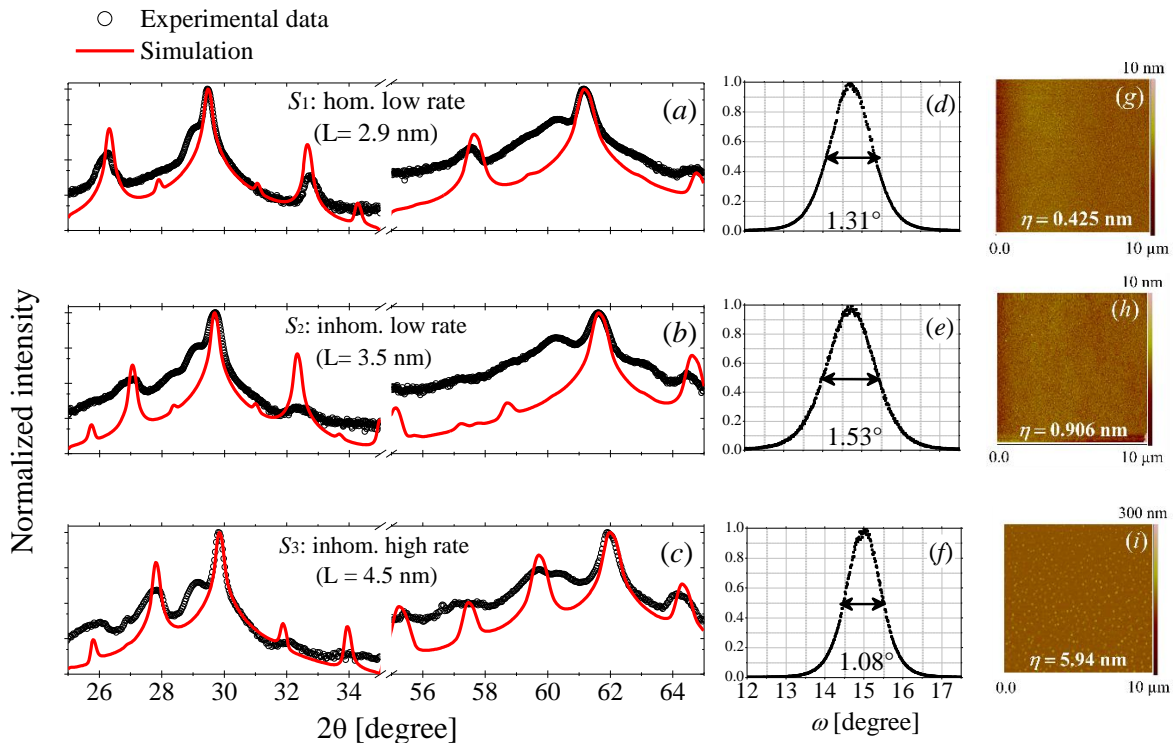


Figure S3 XRD diffractograms (a) to (c), rocking curves (d) to (f) and AFM surface scans (g) to (h) of 37 periods half-Heusler SLs grown under different deposition conditions. The calculation of the XRD spectra (red solid lines) was obtained by using CADEM: calculate X-ray diffraction of epitaxial multilayers.¹

Additionally, the XRD diffractograms of SLs with 111 and 148 periods (S_4 and S_5 , respectively) are displayed **Figure S4**. These SLs were grown 30 cm away from the cathode centres with the deposition conditions identical to ones used for S_3 .

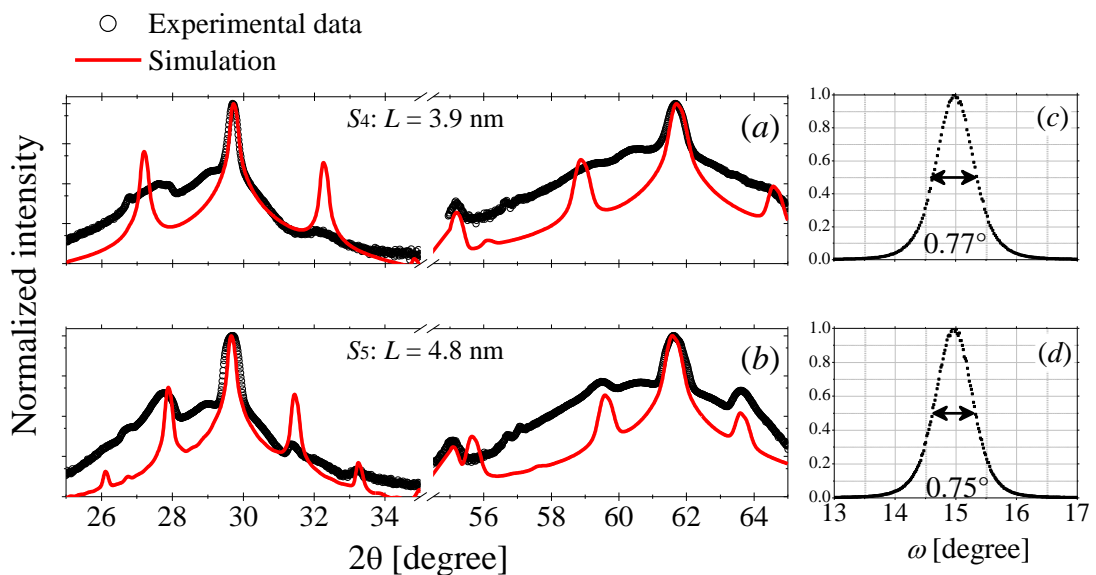


Figure S4 XRD diffractograms (a) and (b), rocking curves (c) and (d) of 111 (S_4 : a and c) and 147 (S_5 : b and d) periods half-Heusler SLs grown under the same deposition conditions as for S_3 . The best fitting theoretical diffractogram models are shown with red lines.¹

Supporting Information

As one can see in **Figure S4** the satellite peaks are weakly accented and the FWHM of the rocking curves decreases with increasing number of periods. That means that the epitaxial quality of the upper parts of the samples must be higher than the one of the lower parts. The period length in this case should be similar but one sees still shifts of the satellite peaks. The roughness rises significantly with the number of periods as one sees in the **Figure S5**.

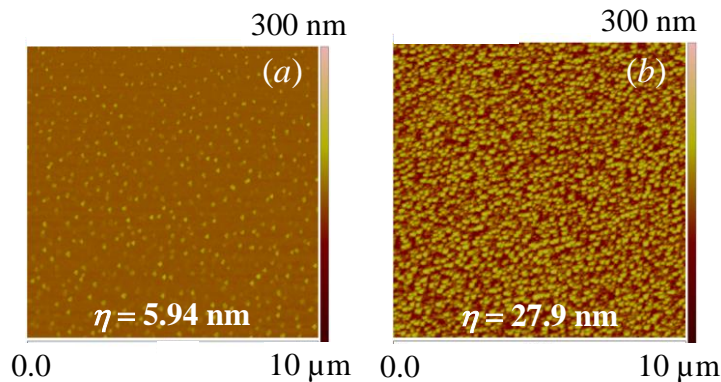


Figure S5 AFM pictures of superlattices grown at high rate parameters in the inhomogeneous region containing: (a) 37, S_3 , and (b) 111, S_4 , periods, respectively.

Finally, the last set of samples was grown using the same conditions as for S_2 but with larger number of periods $N = 111$ (S_6) in single sample holder and using a double sample holder (S_7 and S_8) keeping $N = 37$. In the double sample holder, there is room for two substrates lying side by side so that one substrate was closer to the HfNiSn cathode and the other to the TiNiSn cathode during deposition process. As the samples were grown in the inhomogeneous region, one of the SLs will contain more TiNiSn per period and the other will contain more HfNiSn per period.

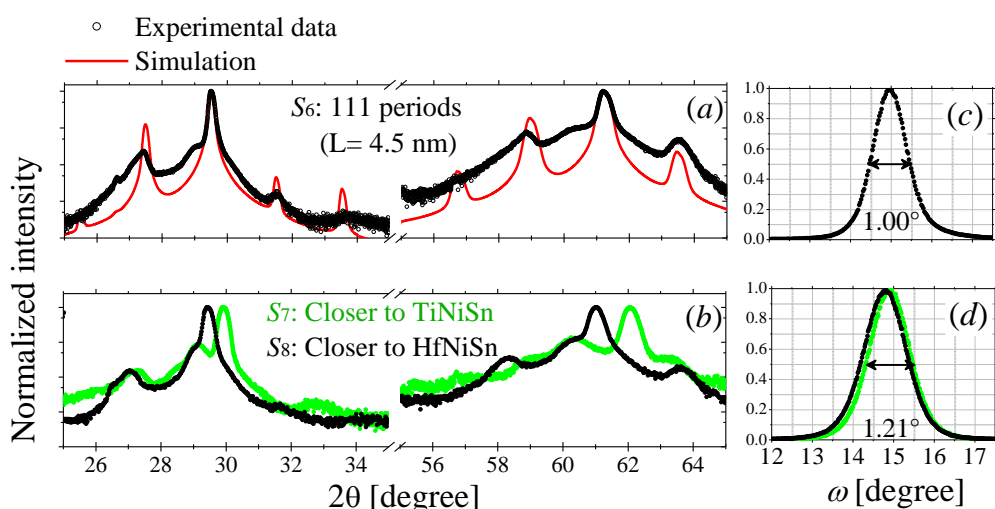


Figure S6 XRD Diffractograms (a) and (b) and rocking curves (c to d) of 111 (S_6 : a and c) and 37 (S_5 : b and d) periods half-Heusler SLs grown under the same deposition conditions of S_2 . The best fitting theoretical diffractogram models are shown with red lines.¹

Supporting Information

The period length of the samples measured here was determined from the best fit of the XRD using CADEM: calculate X-ray diffraction of epitaxial multilayers.¹ Open source and code software to calculate XRD diffractogram of any arbitrary multilayer structure. A summary of all the samples measured in this work is given in **Table S1**.

Table S1 Summary of the deposition parameters, surface roughness, FWHM, and total thickness of investigated samples.

Parameter Sample	d [mm]	p [mbar]	P [W]		N	L [nm]	η [nm]	FWHM [°]	Thickness [nm]	Sample holder
			TNS	HNS						
S_1	0	0.021	7	7	37	2.9	0.425	1.31	108	Single
S_2	30	0.021	7	7	37	3.5	0.906	1.53	107	Single
S_3	30	0.031	24	16	37	4.5	5.94	1.08	159	Single
S_4	30	0.031	24	16	111	3.9	27.9	0.77	450	Single
S_5	30	0.031	24	16	147	4.8	-	0.75	637	Single
S_6	30	0.021	7	7	111	4.5	-	1.00	506	Single
S_7	30	0.021	7	7	37	4.5	-	1.21	107	Double
S_8	30	0.021	7	7	37	4.5	-	1.21	107	Double

2. Three-omega method

The three-omega (3ω) method is an electrothermal technique widely used to determine the thermal conductivity of a specimen. The experiments are performed by inducing harmonic Joule heating in a narrow metal line (3ω -heater), deposited onto the surface of the sample. The metallic strip acts simultaneously as a heater and thermometer due to its temperature dependent electrical resistance as it is displayed in **Figure S7 d**.

In our case, the 3ω -heater was patterned by photolithography and etching of a 50 nm thick gold thin film, grown in situ just after the deposition of AlO_x insulation layer. A schematic representation and a real picture of one the samples is displayed in **Figure S7 a** and **b**, respectively. The deposited metallic strip is composed of four rectangular pads connected by pins to the narrow heating wire. The width of the heating line is defined as $2b = 20 \mu\text{m}$ and the length as $l = 1 \text{ mm}$, the latter being determined by the distance between the inner pads. The outer two pads are used to apply the AC electrical current that generates the Joule heating. The inner two pads are used to measure the voltage, which contains the third harmonic component. In the experiments, a sinusoidal electrical current is applied through the resistive strip as:

$$I_{app}(t) = I_0 \cos(\omega t) \quad (1)$$

where I_0 is the amplitude of the signal.

Supporting Information

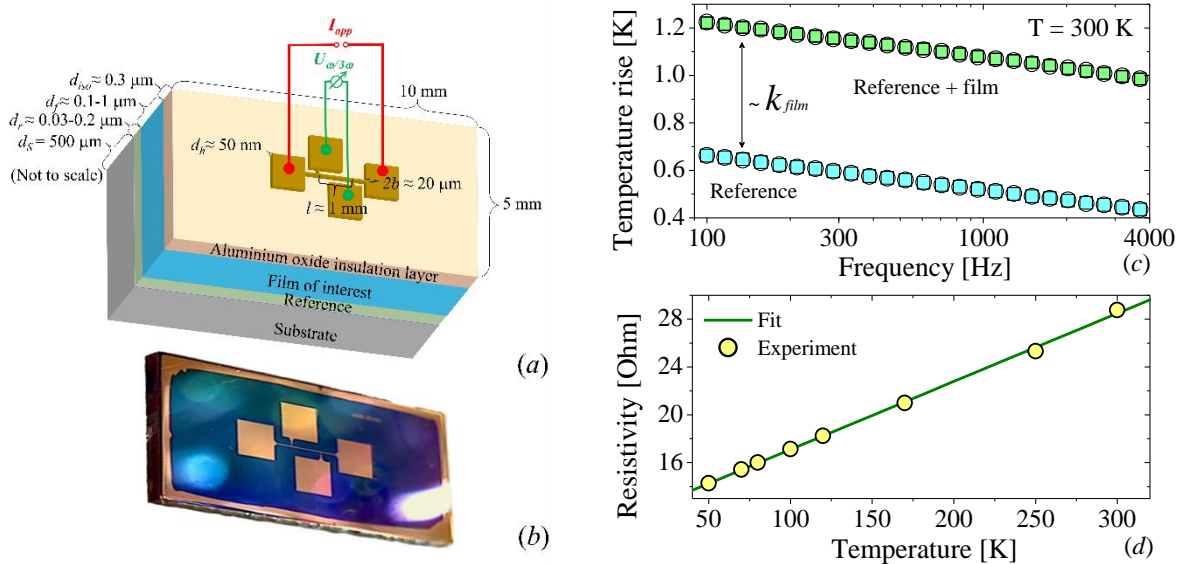


Figure S7 (a) Schematic representation of the samples measured in this work and (b) real picture of one of them. (c) Temperature rise of 3ω -heater vs frequency of $1000 \mu\text{m}$ thick HfNiSn thin film (green squares and empty dots) and its reference (blue square and empty dots). (d) Typical temperature dependence of the electrical resistivity of a 3ω -heater.

By Joule effect, this excitation results in power dissipation that consists of a DC and AC components given by:

$$P(t) = I_{app}(t)^2 R = \frac{I_0^2 R}{2} (1 + \cos(2\omega t)) \quad (2)$$

where R_0 is the resistance of the strip. As the dissipated power has a DC and AC component, the heat dissipation will result in a temperature rise that has a DC (ΔT_{DC}) and an AC (ΔT_{AC}) component. The temperature fluctuation of amplitude $\Delta T_{2\omega}$ will also oscillate at the same frequency.

$$T(t) = \Delta T_{DC} + \Delta T_{AC} \cos(2\omega t + \phi) \quad (3)$$

where ϕ is the phase lag. Since the electrical resistivity is linearly proportional to the temperature (see **Figure S7 c**), the ΔT will also produce a 2ω oscillation in the resistivity as:

$$R(T, t) \approx R_0 (1 + \beta \Delta T_{DC} + \beta \Delta T_{AC} \cos(2\omega t + \phi)) \quad (4)$$

where β is the temperature coefficient of the electrical resistivity of the strip. Now, by applying the Ohm's law, we obtain the modulation of the voltage of the form:

Supporting Information

$$\begin{aligned}
 U &= R(T, t)I(t) \\
 &= I_0 R_0 \cos(\omega t) (1 + \beta \Delta T_{DC} + \beta \Delta T_{AC} \cos(2\omega t + \phi)) \\
 &= U_0 (1 + \beta \Delta T_{DC}) \cos(\omega t) + \frac{U_0 \beta \Delta T_{AC}}{2} (\cos(\omega t + \phi) + \cos(3\omega t + \phi))
 \end{aligned} \tag{5}$$

From (5), one is able to infer the temperature oscillations by measuring the voltage signal at the 3ω frequency^{2,3}:

$$\Delta T_{AC} = \Delta T_{2\omega} = \frac{2U_{3\omega}}{\beta U_0} \approx \frac{2U_{3\omega, rms}}{\beta U_{\omega, rms}} \tag{6}$$

Since the 3ω response of the voltage is very small in comparison with 1ω , the lock-in technique is required to extract the signal. The thermal fluctuation can therefore be obtained from the 3ω component in terms of root mean square quantities (rms), as usually measured by lock-in amplifier. Due to the difference among 1ω and 3ω is several orders of magnitude, the noise of the whole 1ω signal is in the same order as the 3ω signal itself. To avoid this problem, $U_{3\omega}$ is not measured directly at the inner pads of the heater but rather with a passive circuit.

The thermal conductivity can be obtained by solving the transient heat conduction equation for a finite width line heater, deposited onto semi-infinite surface of a film-on substrate system. The temperature rise is given by:

$$\Delta T_{2\omega} = \frac{P}{lk\pi} \int_0^\infty \frac{\sin^2(xb)}{(xb)^2 \sqrt{x^2 + q^2}} dx \tag{7}$$

where P is the applied power, $q \equiv 1/\lambda = \sqrt{2\omega/\alpha}$ is the inverse of the thermal penetration depth (λ), α is the thermal diffusivity and k is the thermal conductivity of the material. The Eq. (7) does not have an analytical solution, however, Cahill^{2,3} showed that for $\lambda \gg b$ the heater can be seen as line source. Then, the upper limit of the integral can be replaced by $1/b$ and the sinusoidal term goes $\sin(xb)/(xb) \sim 1$ in the limit of $b \rightarrow 0$. By introducing these approximations, the analytical solution is given by:

$$\Delta T_{2\omega} = \frac{P}{2lk\pi} \left(-\ln(2\omega) + \ln\left(\frac{k}{\alpha b^2}\right) + 2\gamma \right) - \frac{iP}{4kl} \tag{8}$$

where γ is constant. Finally, the k can be extracted from the slope of the real part of temperature rise vs $\ln(2\omega)$:

Supporting Information

$$k \approx \frac{P}{2\pi d} \left(\frac{d \ln(\Delta T_{2\omega})}{d \ln(2\omega)} \right)^{-1} \quad (9)$$

This approximation of the 3ω measurement is known as slope method. In the following section the errors associated to the slope method are discussed and analyzed for our particular case. For an extended and detailed description on the derivation errors, mathematical expressions and the methodology used to calculate it, the readers are referred to the work of H.S. Carslaw and J.C. Jaeger⁴, D. Cahill^{2,3}, Borca-Tasciuc et al.⁵ C. Dames⁶ and references therein.

2.1 Errors from mathematical description

There are three main requirements that the system has to hold to apply directly the slope method, those are: the heater is a line source, the substrate thickness is semi-infinite and the heater is infinitely long. As the real heater is not infinitesimal narrow and infinitely long in comparison to finite thick substrate. There are some limits where these considerations are valid and they are summarized in the Figure S8. As one can see in Figure S8, in our measurements, it is always possible to choose frequencies for the 3ω method to fulfil the criteria needed for the slope method, with errors below 5%.

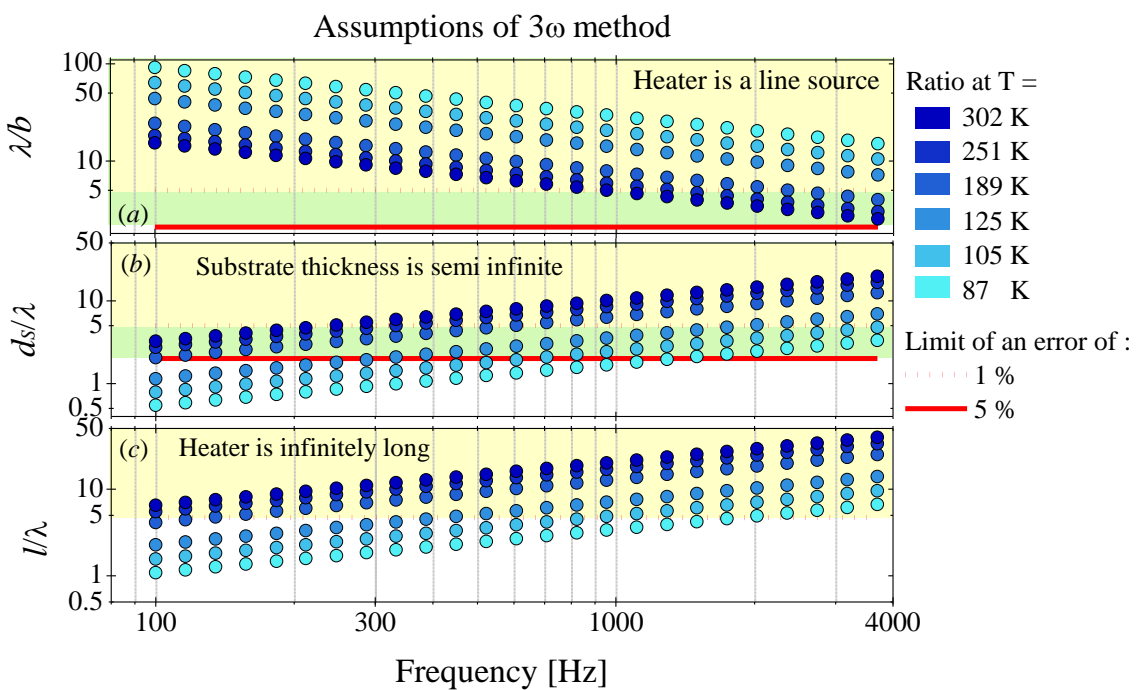


Figure S8 Calculated ratios and criteria for the adequacy of the applied mathematical model for our 3ω measurements: (a) the heater is a line source, (b) the substrate thickness is infinite and (c) the heater line is infinitely long. A point fulfills a criteria if it is above the red lines in the yellow or green rectangle for an error below 1% and 5%, respectively. The substrate capacity and conductivity values that were needed to calculate the substrate penetration depth were taken from reference.⁷ The criteria are taken from Ref. ⁶.

Supporting Information

2.2 Differential method: determination of the k of a thin film

Once we ensure that the slope method can be applied in our substrates, the next step is calculation estimation of k of the film of interest by using the 3ω differential method.^{8,9} In case of a film that has a conductivity much smaller than the substrate and a heater width that is larger than the film thickness, one can model the film as a frequency independent resistance where the bigger part of the heat flows cross plane from heater-film-interface to film-substrate-interface.⁸ In this case the Fourier law can be applied in one dimension:

$$P = Q = kA_{\text{int}} \frac{\Delta T_f}{d_f} \approx 2klb \frac{\Delta T_f}{d_f} \quad (10)$$

$$\Rightarrow k = \frac{Pd_f}{2lb\Delta T_f}$$

where Q is the modulus of the heat flow, A_{int} is the area below the heater strip ($A_{\text{int}} = 2lb$) and ΔT_f is the temperature rise of the film. Since the 3ω measurement gives only the temperature difference oscillation amplitude between top (interface heater-sample) and bottom (interface of sample to the infinite sink) of the whole sample, it is not possible to measure ΔT_f directly. But if one creates a film that consists not only of the film of interest but adds a small reference, the measurable quantity temperature rise of the system (ΔT_{sys}) can be super-posed by the ΔT_f and the ΔT_r of the system containing the substrate and the reference (see **Figure S7 a**). Then the temperature rise of the system can be expressed as:

$$\Delta T_{\text{sys}} = \Delta T_r + \Delta T_f \quad (11)$$

The ΔT_r is obtained directly by measuring other sample that contains only the substrate and the reference film. Finally, the thermal conductivity of the film of interest is obtained by subtracting the ΔT_{sys} and ΔT_f and given by:

$$k = \frac{Pd_f}{2bl(\Delta T_{\text{sys}} - \Delta T_r)} \quad (12)$$

Therefore, for each film-on-substrate measurement, it is required to create and measure at least two samples, namely one sample containing the film of interest as well as a reference part and a second sample containing only the reference part (see **Figure S7 c**). Naturally both reference parts need to be created under similar conditions on equal substrates. In our case the reference consisted of 5 nm of vanadium and 25 nm of HfNiSn buffer layers. It is important to mention that as the width of the heater line is not exactly the same in each sample, a correction of the ΔT must to be applied as follows:

Supporting Information

$$\Delta T_c = \frac{b_{mask}}{b_{measured}} \Delta T = c_b \Delta T \quad (13)$$

The correction takes into account the deviation in heater width due to the photolithographic processes. This quantity was estimated through image analysis of five pictures taken with an optical microscope using a 100x objective along of the 3ω -strip.

To perform a T measurement with this method, one needs to create a difference of T without a significant ΔT in the substrate. The error given by this simplification is less than 1%, if the ratio $(k_f/k_s)^2 < 0.01$. In our case all observed $k_f < 5 \text{ W/(K m)}$ and the lowest observed $k_s \approx 50 \text{ W/(K m)}$, then, this criteria is fulfilled for all measurements.⁶ The error propagation for the differential method leads to errors about 5%, a mathematical error in this range is tolerable here and the line source criteria does not need to be fulfilled as strictly as for the slope method. To achieve an error lower than 5% the ratio $\lambda/b \leq 2.1$ and for an adequate semi-infinite substrate assumption d_s/λ must be bigger than two. The complete requirements for these approximations are shown in **Figure S8**.

2.3 Estimation of measurement errors for thin film measurements

For the measurements done in this work, it was always tried to keep the errors caused by the mathematical model as low as possible by choosing an adequate frequency range for present environment temperature. Therefore, the line source assumption and the semi-infinite substrate assumption were taken into account as well as the infinitely long heater assumption. It is not possible to find a range where all limits for an error lower than 1% are fulfilled at the same time for all the temperatures. One reason for this is the fact that the line source criterion behaves in a different way as a function of temperature than the other two criteria. But we can be sure, that the errors caused by mathematical assumptions are always below 5%.

Supporting Information

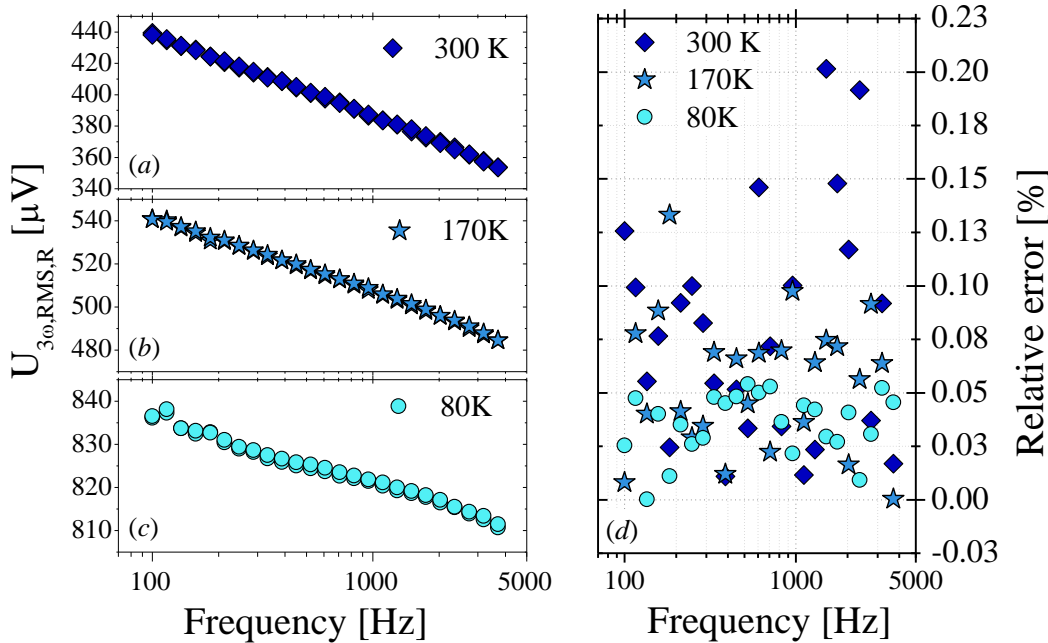


Figure S9 Measured three omega voltages (a) to (c) and relative error (d) at each frequency for $1\mu\text{m}$ thick HfNiSn thin film at three different temperatures $T = 300$ (a), 170 (b) and 80 (c) K for fixed power $P = 20$ mW. The estimations done by the mathematical model are not the only possible sources of errors. The 3ω -method requires several measurements of electrical and geometrical quantities that contain statistical errors that will affect the result as shown in **Table S2** and **Table S3**.

Table S2 Relative errors of the measured electrical quantities of the used 3ω -method. The errors for R_0 and P can be calculated with this values using error propagation.

$\delta_{\text{rel}} dR/dT$	$\delta_{\text{rel}} U_{\omega,RMS}$	$\delta_{\text{rel}} I_{\omega,RMS}$	$\delta_{\text{rel}} U_{3\omega,RMS}$
0.5 %	0.1 %	0.1 %	0.3 %

In contrast to the other measured quantities, the determination of the third omega signal $U_{3\omega,RMS}$ is not straightforward. Therefore one needs to explain how the errors are determined in this case. For each sample at each measured temperature, the chosen frequency range is measured at least twice. The error was determined by the deviation of both measured points. An example for this praxis is showed in **Figure S9**. The deviation of a point at each frequency leads to relative errors less than 0.2% in this example. The highest relative error of $U_{3\omega,RMS}$ measured in this work was 0.3%.

Table S3 Relative errors of the measured geometrical quantities of the used 3ω -method.

$\delta_{\text{rel}} d$	$\delta_{\text{rel}} l$	$\delta_{\text{rel}} b$	$\delta_{\text{rel}} c_b$
2.0 %	0.5 %	Expressed in c_b	1.0 %

The propagation of uncertainty is done below for the absolute error δx of the general quantity x . The single quantities are assumed as uncorrelated. As an example, the error propagation for the temperature coefficient of the resistance β is calculated below:

Supporting Information

$$\delta\beta = \sqrt{\left(\frac{\delta dR/dT}{R_0}\right)^2 + \left(\frac{\delta R_0 dR/dT}{R_0^2}\right)^2} \quad (14)$$

The error propagation for the corrected temperature oscillation amplitude $\delta\Delta T_c$ can be written as:

$$\delta\Delta T_c = 4 \left[\frac{c_b^2 \delta U_{\omega,RMS}^2 U_{3\omega,RMS}^2}{\beta^2 U_{\omega,RMS}^4} + \frac{c_b^2 \delta \beta^2 U_{3\omega,RMS}^2}{\beta^4 U_{\omega,RMS}^2} \right. \\ \left. + \frac{c_b^2 \delta U_{\omega,RMS}^2}{\beta^2 U_{\omega,RMS}^2} + \frac{\delta c_b^2 U_{3\omega,RMS}^2}{\beta^2 U_{\omega,RMS}^2} \right]^{1/2} \quad (15)$$

The error propagation for the k of the differential method can be expressed as:

$$\delta k = \left[\frac{d_f^2 \delta l^2 P^2}{4b^2 l^4 (\Delta T_{sys,c} - \Delta T_{r,c})^2} + \frac{d_f^2 \delta \Delta T_{r,c}^2 P^2}{4b^2 l^2 (\Delta T_{sys,c} - \Delta T_{r,c})^4} + \frac{d_f^2 \delta \Delta T_{sys,c}^2 P^2}{4b^2 l^2 (\Delta T_{sys,c} - \Delta T_{r,c})^4} \right. \\ \left. + \frac{d_f^2 \delta P^2}{4b^2 l^2 (\Delta T_{sys,c} - \Delta T_{r,c})^4} + \frac{\delta d_f^2 P^2}{4b^2 l^2 (\Delta T_{sys,c} - \Delta T_{r,c})^2} \right]^{1/2} \quad (16)$$

Due to the mathematical expressions for β and ΔT_c only contain products, the relative errors $\delta_{rel}x = \delta x/x$ can be expressed as:

$$\delta_{rel}\beta = \frac{\delta\beta}{\beta} = \sqrt{(\delta_{rel}dR/dT)^2 + (\delta_{rel}R_0)^2} \quad (17)$$

$$\delta_{rel}\Delta T_c = \frac{\delta\Delta T_c}{\Delta T_c} = \sqrt{(\delta_{rel}c_b)^2 + (\delta_{rel}U_{\omega,rms})^2 + (\delta_{rel}U_{3\omega,rms})^2 + (\delta_{rel}\beta)^2} \quad (18)$$

One sees here, that the relative error of ΔT_c depends only on the relative errors of measurement instruments. Usually, it is possible to assume that the relative error of an instrument only depends on the chosen measurement scale. Then, if one uses the same scale for each measured sample, the relative error does neither depend on the single measured value of a quantity nor on the measured sample. Therefore, we can assume that the relative error $\delta_{rel}\Delta T_c$ is constant for each measurement. The case is different for the k , because, k contains the difference $(\Delta T_{sys,c} - \Delta T_{r,c})$, thus it cannot be expressed just in terms of relative errors and therefore does not stay constant. But, the largest part of it can be expressed with relative measurement errors, so that it shows only a dependence on the ratio $\Delta T_{sys,c}/\Delta T_{r,c}$:

Supporting Information

$$\delta_{rel}k = \frac{\delta k}{k} = \left[(\delta_{rel}d_f)^2 + (\delta_{rel}l)^2 + (\delta_{rel}P)^2 + (\delta_{rel}\Delta T_{r,c})^2 (\Delta T_{sys,c} / \Delta T_{r,c} - 1)^{-2} + (\delta_{rel}\Delta T_{sys,c})^2 (1 - (\Delta T_{sys,c} / \Delta T_{r,c})^{-1})^{-2} \right]^{1/2} \quad (19)$$

In **Figure S10** this function is plotted for the instrument errors shown in **Table S2** and **Table S3**. Notice that the relative error of k decreases with increasing $\Delta T_{sys,c}/\Delta T_{r,c}$. Therefore, it is advisable to grow samples with a thickness difference between reference and film of interest as large as possible. In this way it is warranted that the ΔT ratio is large enough. It is important to notice that the $\Delta T_{sys,c}/\Delta T_{r,c}$ is also dependent on the difference of k between reference and film of interest, then, it will not be similar for samples with equal thickness. In our work the $\Delta T_{sys,c}/\Delta T_{r,c}$ is close to 1.5 for most of the samples measured in this work. This leads to errors between 4 and 7%.

For all the measurements carried out in this work, at least two measurement points of $U_{3\omega,rms}$ were taken for similar conditions of the same sample (See **Figure S7 c**). In this way, one can see statistical deviations as well as the errors calculated with error propagation. This statistical deviations are much smaller than the error bars calculated with the Eq. (19), because they only depend on deviations of $U_{3\omega,rms}$ while the error propagation takes several additional error sources into account. Therefore the error propagation is more feasible than considering simply the statistical errors of $U_{3\omega,rms}$.

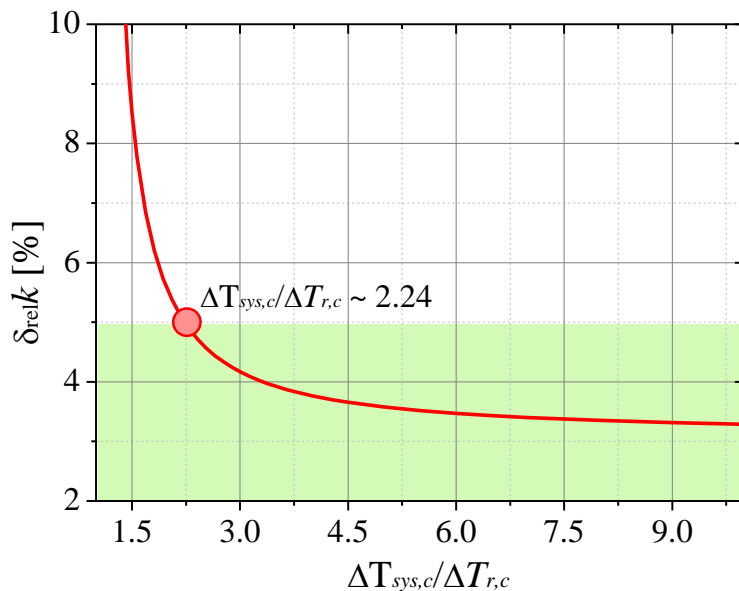


Figure S10 Relative error of the thermal conductivity for the differential method in dependence of the ratio $\Delta T_{sys,c}/\Delta T_{r,c}$. The curve is dependent on the relative errors of the measured quantities. This curve was calculated for the estimated errors of the 3ω setup used in this work.

Supporting Information

3 Calculation of amorphous limit of the thermal conductivity

The lowest thermal conductivity value for semiconductors and insulating materials is achieved for the systems with the small order what is similar to the amorphous state. The pioneer theoretical framework on heat conduction in amorphous materials was first proposed by Einstein¹⁰, refined by Slack¹¹ and extended by Cahill *et al.*¹² The theory is basically based on the assumption of that heat conduction is described by a “random walk” of independent oscillators with a characteristic frequency (Einstein frequency). Then, each atom is coupled to its first-, second-, and third nearest neighbors on a simple cubic lattice by harmonic forces. Slack reformulated this problem by considering that the minimum MFP (Λ) of a heat carrier has to be the same as its wavelength (λ), namely $\Lambda = \lambda$.¹¹ The k estimated by this model is known as the minimum thermal conductivity or amorphous limit (k_{\min}). Following both works, Cahill *et al.*¹² further extended this model by dividing the system into regions of size $\lambda/2$, with a constant velocity given by the Debye speed of sound. Then, the Λ of each oscillator is assumed to be $\lambda/2$. Finally, the k is reformulated in terms of sum of three Debye integrals as follows¹²:

$$k_{\min} = \left(\frac{\pi}{6} \right)^{1/3} k_B n^{2/3} \sum_j v_j \left(\frac{T}{\Theta_{D,j}} \right)^2 \int_0^{\Theta_{D,j}/T} \frac{x^3 e^x}{(e^x - 1)^2} dx \quad (20)$$

where Σ_j represents the sum on longitudinal (L) and transverse (T) polarizations, n is the number density of atoms (i.e., n = number of atoms in a unit cell / volume of unit cell), k_B is the Boltzmann constant, $\Theta_{D,i}$ is the Debye temperature given by:

$$\Theta_{D,i} = \frac{h v_i}{2 \pi k_B} (6 \pi^2 n)^{1/3} \quad (21)$$

where h is the Planck constant. The **Table S4** summarizes all the parameters used in this work to calculate the amorphous limit of the HH compounds.

Table S4 Parameter used to estimate the amorphous limit of the thermal conductivity of the HHs compounds.

Parameter	TiNiSn	HfNiSn
v_L	5952 [m/s] ¹³	4195 [m/s] ¹⁴
v_T	3427 [m/s] ¹³	2783 [m/s] ¹⁴
a	0.5941 [nm] ¹⁵	0.6083 [nm] ¹⁶
Number of atoms per unit cell	12	12

Supporting Information

The amorphous limit of the effective material was calculated as the reciprocal of the average of the minimum thermal conductivities. The temperature dependence of the amorphous limit for each compound is displayed in **Figure S11**.

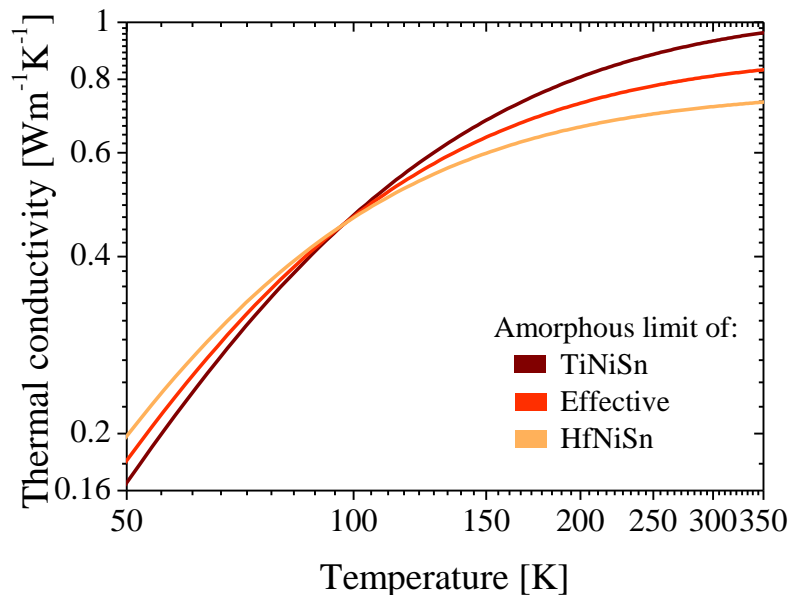


Figure S11 Amorphous limit of the different HH compounds and the effective material.

References

- (1) Komar, P.; Jakob, G. CADEM : Calculate X-Ray Diffraction of Epitaxial Multilayers. *J. Appl. Crystallogr.* **2017**, *50* (1), 288–292.
- (2) Cahill, D. G. Thermal Conductivity Measurement from 30 to 750 K: The 3ω Method. *Rev. Sci. Instrum.* **1990**, *61* (2), 802.
- (3) Cahill, D. G. Erratum: “Thermal Conductivity Measurement from 30 to 750 K: The 3ω Method” [Rev. Sci. Instrum. 61, 802 (1990)]. *Rev. Sci. Instrum.* **2002**, *73* (10), 3701.
- (4) Carslaw, H. S. ; Jaeger, J. C. . The Flow of the Heat in an Infinite Circular Cylinder. In *Conduction of Heat in Solids*; Oxford University Press: London, 1959; pp 188–214.
- (5) Borca-Tasciuc, T.; Kumar, A. R.; Chen, G. Data Reduction in 3ω Method for Thin-Film Thermal Conductivity Determination. *Rev. Sci. Instrum.* **2001**, *72* (4), 2139–2147.
- (6) Dames, C. Measuring the Thermal Conductivity of Thin Films: 3 Omega and Related Electrothermal Methods. *Annu. Rev. Heat Transf.* **2013**, *16* (1), 7–49.
- (7) Cahill, D. G. . Thermal conductivity bulk single crystal MgO; Temperature dependence of volumetric heat capacity MgO. Department of Materials Science and Engineering. University

Supporting Information

of Illinois at Urbana Campaign <http://users.mrl.illinois.edu/cahill/tcdata/tcdata.html> (accessed Jan 1, 2016).

- (8) Cahill, D.; Katiyar, M.; Abelson, J. Thermal Conductivity of a-Si:H Thin Films. *Phys. Rev. B* **1994**, *50* (9), 6077–6081.
- (9) Kim, J. H.; Feldman, A.; Novotny, D. Application of the Three Omega Thermal Conductivity Measurement Method to a Film on a Substrate of Finite Thickness. *J. Appl. Phys.* **1999**, *86* (7), 3959–3963.
- (10) Einstein, A. Elementare Betrachtungen Über Die Thermische Molekularbewegung in Festen Körpern. *Ann. Phys.* **1911**, *340* (9), 679–694.
- (11) Slack, G. A. The Thermal Conductivity of Nonmetallic Crystals. In *Solid State Physics Vol. 34*; Ehrenreich, H., Seitz, F., Turnbull, D., Eds.; Academic Press: New York, San Francisco & London, 1979; pp 1–71.
- (12) Cahill, D. G.; Watson, S. K.; Pohl, R. O. Lower Limit to the Thermal Conductivity of Disordered Crystals. *Phys. Rev. B* **1992**, *46* (10), 6131–6140.
- (13) Hichour, M.; Rached, D.; Khenata, R.; Rabah, M.; Merabet, M.; Reshak, A. H.; Bin Omran, S.; Ahmed, R. Theoretical Investigations of NiTiSn and CoVSn Compounds. *J. Phys. Chem. Solids* **2012**, *73* (8), 975–981.
- (14) Özisik, H.; Çolakoglu, K.; Özisik, H. B. Ab-Initio First Principles Calculations on Half-Heusler NiYSn (Y=Zr, Hf) Compounds Structural, Lattice Dynamical and Thermodynamical Properties. *AJP Fiz.* **2010**, *16* (2), 154–157.
- (15) Romaka, V. V.; Rogl, P.; Romaka, L.; Stadnyk, Y.; Melnychenko, N.; Grytsiv, A.; Falmbigl, M.; Skryabina, N. Phase Equilibria, Formation, Crystal and Electronic Structure of Ternary Compounds in Ti–Ni–Sn and Ti–Ni–Sb Ternary Systems. *J. Solid State Chem.* **2013**, *197*, 103–112.
- (16) Larson, P.; Mahanti, S. D.; Kanatzidis, M. G. Structural Stability of Ni-Containing Half-Heusler Compounds. *Phys. Rev. B* **2000**, *62* (19), 12754–12762.